OPEN ACCESS
IOP Publishing
Journal of Physics D: Applied Physics
J. Phys. D: Appl. Phys. **58** (2025) 435205 (12pp)
https://doi.org/10.1088/1361-6463/ae1300

2D photofragmentation LIF imaging of H_2O_2 and HO_2 in the effluent of an atmospheric-pressure plasma jet: effects of solid and liquid interfaces

María J Herrera Quesada[1], **Sebastian Pfaff**[2], **Jordyn Polito**[3], **Mark J Kushner**[4], **Jonathan H Frank**[2] and **Katharina Stapelmann**[1,*]

[1] Department of Nuclear Engineering, North Carolina State University, Raleigh, NC, United States of America
[2] Combustion Research Facility, Sandia National Laboratories, Livermore, CA, United States of America
[3] Department of Chemical Engineering, University of Michigan, Ann Arbor, MI, United States of America
[4] Department of Electrical Engineering and Computer Science, University of Michigan, Ann Arbor, MI, United States of America

E-mail: kstapel@ncsu.edu

Received 5 August 2025, revised 28 September 2025
Accepted for publication 14 October 2025
Published 24 October 2025

Abstract

Two-dimensional (2D) absolute measurements of hydrogen peroxide (H_2O_2) and approximations of the hydroperoxyl radical (HO_2) in the effluent of a COST Reference Microplasma Jet operated with a He/H_2O feed gas are presented. Gas-phase densities are mapped using photofragmentation laser-induced fluorescence (PF-LIF) under three boundary conditions: open effluent, a solid target, and a liquid target. A novel method is presented for separating PF-LIF signals from H_2O_2 and HO_2 using comparative measurements in oxygen-rich and oxygen-free environments to exploit the preferential formation of HO_2 in the presence of molecular oxygen. This separation strategy is supported by results from a plug-flow plasma chemistry model. Measured densities agree closely with model predictions in both magnitude and trend, while the 2D experimental distributions provide additional insight into the spatial dependencies of these species. In particular, the results show distinct differences in species transport depending on the target type: solid surfaces induce lateral deflection and reduced centerline densities, whereas liquid interfaces promote axial accumulation and higher near-axis concentrations.

* Author to whom any correspondence should be addressed.

Supplementary material for this article is available online

Keywords: atmospheric-pressure plasma jet (APPJ), photofragmentation (PF), laser-induced fluorescence (LIF), hydrogen peroxide (H_2O_2), hydroperoxyl radical (HO_2), plasma chemistry model, plasma surface and liquid interactions

1. Introduction

Reactive oxygen and nitrogen species (RONS) produced by atmospheric-pressure plasmas are central to a wide range of biological, chemical, and medical applications, where their controlled production and transport influence processes such as enzymatic reactions, wound healing, sterilization, and oxidative stress-related therapies [1–3]. Among these species, hydroxyl radicals (OH), hydrogen peroxide (H_2O_2), and hydroperoxyl radicals (HO_2) play key roles. OH is one of the most reactive species produced in plasma environments, contributing to antimicrobial activity, oxidative modification of biomolecules, and the initiation of radical-driven reaction cascades [4–6]. H_2O_2, while less reactive than OH, serves as a key mediator in plasma-liquid interactions and is widely used in medical disinfection, tissue regeneration, and enzymatic processes [2, 7]. The lower reactivity of H_2O_2 extends its lifetime in solution, making it more likely to accumulate and transport in applications. HO_2 is an intermediate species in the conversion between OH and H_2O_2 that plays a crucial role in the oxidative balance of plasma environments [8]. The relationships between these species influence plasma-driven biochemical pathways.

An improved understanding of the role of OH, HO_2, and H_2O_2 in plasma interactions with solid and liquid interfaces is particularly important for applications such as plasma-assisted wound healing and plasma-liquid chemistry for biomedical processes [9, 10]. When plasma-generated RONS come into contact with a solid or liquid interface, their transport and reactivity can be significantly altered, affecting their availability in biological or chemical systems [11, 12]. However, spatially resolved measurements of species densities near interfaces pose substantial challenges. Diagnostics often lack sufficient spatial resolution or introduce perturbations, conditions that compromise the accuracy of near-surface measurements [13, 14]. For example, optical emission and absorption spectroscopy provide inherently line-integrated measurements, resulting in spatial and temporal averaging that hinders accurate resolution of steep density gradients [15–18]. Molecular beam mass spectrometry provides sensitive universal species detection but is typically limited to measurement of species directly intersecting with surfaces. In contrast, laser imaging diagnostic techniques can provide spatially resolved measurements without significantly disturbing the plasma or its interactions with a surface.

Laser-induced fluorescence (LIF) is a widely used technique for spatially resolved imaging of species that have compatible absorption and emission transitions. Our recent study used OH-LIF imaging to investigate two-dimensional (2D) distributions of OH densities in the effluent of the COST Reference Microplasma Jet (COST-Jet) as the plume interacts with solid surfaces [19]. To provide a more complete picture of reactive oxygen species (ROS) in the COST-Jet effluent, complementary measurements of H_2O_2 and HO_2 were performed with the effluent propagating into an open atmosphere and interacting with solid and liquid surfaces. However, these species are directly inaccessible by LIF because their electronically excited states are highly predissociative. Instead, photofragmentation-LIF (PF-LIF) is used to detect HO_2 and H_2O_2. In this pump-probe technique, HO_2 and H_2O_2 are first photodissociated by a pump laser, resulting in photolytic production of either one or two OH molecules, respectively. The OH photofragments are then detected using a probe laser for OH-LIF measurements. This technique has been used in combustion and plasma applications [20–23].

In this study, PF-LIF measurements of the 2D distributions of absolute H_2O_2 densities in the effluent of the COST-Jet operated with a He/H_2O admixture in N_2 and air environments were performed. These measurements were then used to estimate corresponding HO_2 density distributions by developing an approach to separate the contributions of H_2O_2 and HO_2 to the PF-LIF signals. The experimentally determined densities align closely with predictions from a zero-dimensional (0D) plug-flow plasma chemistry model. The 2D maps reveal the formation of 'reaction fronts' where the plasma effluent interacts with ambient air, as well as the influence of target boundary conditions on species transport. When the COST-Jet plume impinges on a fused silica (FS) disk, radicals are deflected outward, decreasing centerline densities, whereas impingement on liquid water produces narrower horizontal distributions and higher centerline densities of both H_2O_2 and HO_2. These spatially resolved observations, enabled by coupling of the PF-LIF technique with chemical kinetic modeling, provide insights into the modulation of ROS at plasma-interface boundaries.

2. Experimental setup

2.1. Plasma source

The COST-Jet is a capacitively coupled atmospheric-pressure plasma source sustained by radio frequency (RF) excitation at 13.56 MHz. A comprehensive description of its design and functionality can be found in Golda *et al* [24]. The device features electrodes 30 mm in length and 1 mm wide, positioned 1 mm apart, resulting in a plasma volume of 30 mm^3.

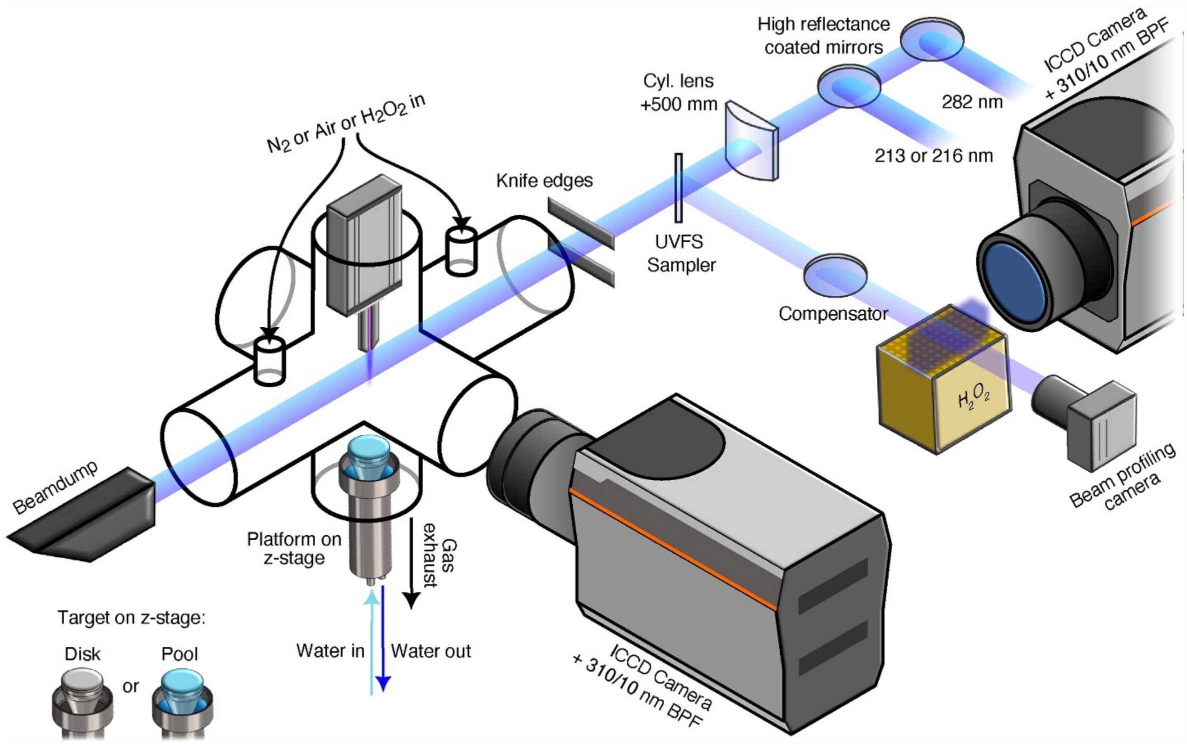

Figure 1. Experimental setup. The excitation laser beam for OH-PLIF (282 nm) is overlapped with the H_2O_2 photodissociation laser beam (213 nm or 216 nm) by using high-reflectance mirrors. Both beams are formed into thin sheets by a +500 mm cylindrical lens. A UV-fused silica (UVFS) beamsplitter diverts a small fraction of the beams into a controlled flow of H_2O_2 and a beam profiling camera for real-time beam monitoring. The main beams are cropped by a knife edge before entering the six-way glass cross, where they traverse the central axis of the COST-Jet effluent and finally terminate at a beam dump. The PF-LIF signal is recorded by an ICCD camera equipped with a 310/10 nm band-pass filter. Downstream of the cross, a movable platform carrying either a solid (FS disk) or liquid (water) target can be raised to specified distances from the jet nozzle.

In the present experiments, helium was used as the primary feed gas to the jet, with controlled addition of water vapor at a concentration of 0.25%. The total gas flow rate for the He/H_2O admixture was maintained at 1 slm. High-purity helium (Matheson Ultra-High Purity, 99.999%) was used. The humidified helium mixture was produced by directing 108 sccm of dry helium through a water bubbler kept in a temperature-controlled water bath at 20 °C. The humidified helium was then combined with 892 sccm of dry helium, yielding a final water mole fraction of 0.25%.

The plasma jet power was stabilized at 750 ± 10 mW and continuously monitored using an oscilloscope connected to the internal current and voltage probes of the COST-Jet. The plasma jet was housed within a six-way glass cross, as shown in figure 1. The cross had an internal diameter of 5 cm and leg lengths of 8 cm and 13 cm, oriented perpendicular and parallel to the laser beam, respectively. The COST-Jet was mounted on the upper port, while a translation stage, optionally equipped with a solid (2.5 cm diameter FS disk) or liquid target (2.5 cm diameter water reservoir/pool), was mounted through the bottom port. Openings around the stage and target allowed gases to flow out of the cross. Optical access was provided through quartz ultraviolet-FS (UVFS) windows that sealed the remaining ports.

To maintain a stable meniscus in the water pool and avoid variations in the water level due to evaporation, the liquid was continuously circulated using a pump system configured with a trickle flow. This system ensured a consistent water level while maintaining a quiescent surface throughout the experiment. The water reservoir featured tapered edges to accentuate the meniscus, enabling consistent optical access and minimizing surface distortion from possible volume changes.

Encasing the jet within the six-way cross enabled environmental control while maintaining atmospheric pressure through the top and bottom outlets. To regulate the atmosphere surrounding the COST-Jet and its effluent, an 8 slm flow of either air or N_2 (4 slm from each of two axisymmetric top inlets) was introduced. The inlets and outlets were sufficiently far from the plasma effluent to prevent any significant disturbances of the jet flow. The nitrogen flow was sourced from evaporated liquid nitrogen, while air was supplied via the house air compressor, which may have introduced slight variations in ambient humidity. For calibration, the cross was filled with uniform concentrations of H_2O_2 vapor or acetone as a fluorescent tracer gas.

2.2. PF-LIF for hydrogen peroxide and the hydroperoxyl radical

The PF-LIF setup for the optical detection of H_2O_2 and HO_2 is similar to that presented in [25] and is shown in figure 1. The H_2O_2/HO_2 detection uses a pump-probe technique, where a pump laser ($\lambda = 213$ nm or 216 nm) dissociates H_2O_2 and HO_2 to form OH molecules, and the OH photofragments are detected using a probe laser ($\lambda = 282$ nm) to excite LIF.

Both the native OH in the jet and the OH generated via PF of HO_2 and H_2O_2 are excited by the probe laser, which is tuned to the $Q_1(1)$ rotational transition in the A←X (1,0) band at 281.996 nm (referred to as 282 nm). This transition is well suited for OH-LIF measurements because it combines a high line strength with spectral isolation, and its $N = 1$ rotational state is significantly populated under the plasma temperatures studied; all reasons why it has been employed in earlier OH-LIF/PF-LIF work [19, 21, 25]. To isolate the contribution of photolytically produced OH, the native OH-LIF signal is subtracted; further details on the native OH in this plasma source and gas admixture are provided in Quesada *et al* [19].

The pump and probe lasers operated at a pulse repetition rate of 10 Hz. For the experiments involving targets, a 216 nm laser was used as the pump laser, whereas a 213 nm laser was used for the open effluent experiments. This choice was due to the availability of the lasers at the time of the respective experiments. The absorption cross-sections of H_2O_2 and HO_2 at 216 nm and 213 nm differ by less than 10% [26, 27], allowing for this flexibility in wavelength selection without significant impact on photolysis efficiency.

The 216 nm pump laser beam (4 mJ/pulse) was generated by mixing the output of a dye laser (Continuum ND6000) pumped by the second harmonic of a Nd:YAG laser (Continuum Surelite, $\lambda = 532$ nm) with the third harmonic of the same Nd:YAG laser ($\lambda = 355$ nm), as previously described in [28, 29]. The 213 nm laser beam provided significantly greater energy (12 mJ/pulse) and was produced by 5th harmonic generation of a Nd:YAG laser (Spectra Physics). Calculations based on the fluence of the lasers and the corresponding absorption cross-sections for H_2O_2 yield a PF fraction of $\leqslant 6\%$, which is well below saturation levels.

The 282 nm excitation wavelength is generated using a frequency-doubled dye laser (Lambda-Physik), pumped by the second harmonic of a Nd:YAG laser (Spectra Physics). The resulting OH-LIF emission from the A→X (1,1) and A→X (0,0) bands is detected with an intensified CCD camera (Andor iStar) equipped with a bandpass interference filter centered at 310 nm. A pump-probe delay of 50 ns is used to minimize interference from scattering and broad-spectrum fluorescence generated by the pump laser. The OH-LIF probe laser was operated in the linear excitation regime. This was confirmed by a power-dependence measurement, which is shown in supplemental figure 1.

To correct for variations in OH(A) collisional quenching rates due to local variations in gas composition and temperature, pixel-resolved quenching rate measurements were performed for each atmosphere and geometry (effluent in open ambient conditions or impinging on a solid/liquid target) using the OH radicals produced natively in the plasma jet, following the method in Quesada *et al* [19]. The temporal decay of the OH-LIF signal was measured by acquiring a series of LIF images at different delay times between the 282 nm laser pulse and the image intensifier gate. The resulting temporal decay of the LIF signal at each pixel in the image was fit to an exponential function with the exponential time constant corresponding to the fluorescence lifetime, the reciprocal of the quenching rate. Experimentally determined maps of OH fluorescence lifetimes used for OH-LIF image correction for He/H_2O in open air and N_2 atmospheres are shown in the supplementary information of Quesada *et al* [19]. Because vibrational and rotational energy transfer (VET/RET) processes act during the excited-state lifetime of OH, their influence is inherently included in these pixel-resolved quenching rates and thus accounted for in the calibrated densities reported here.

Variations in optical throughput of the imaging system, including vignetting effects caused by obscuration near the solid or liquid surfaces, as described in [19], were accounted for with flat-field correction measurements by filling the six-way cross with a uniform mixture of acetone and recording acetone LIF signals. Spatial variations in the laser beam profiles that arose during the measurements were corrected by sampling the laser beams with a beamsplitter and directing them through a separate flow of a homogeneous H_2O_2 gas mixture and recording the resulting PF-LIF signal with a second camera. To ensure a consistent spatial overlap of the pump and probe lasers, the sampled laser beams were directed onto a beam profiling camera that monitored their intensity distributions.

For calibration of the H_2O_2 PF-LIF signal, the signal from the jet was compared with a reference signal obtained by performing a PF-LIF measurement using a homogeneous gas flow with a known amount of H_2O_2. The H_2O_2 was produced by passing Ar through a bubbler filled with a 50 wt% H_2O_2 solution in water. The H_2O_2 density in the bubbler exhaust was determined using optical absorption measurements. The bubbler exhaust flowed through a 33 cm absorption cell, where the absorbance of the pump laser was measured after four passes through the cell. To estimate the HO_2 densities, the H_2O_2 calibration was scaled by an efficiency factor to account for the greater sensitivity of the PF-LIF technique to HO_2, as discussed in section 3.1.

2.3. 0D plasma chemistry model

GlobalKin is a 0D plasma kinetic model designed to simulate flowing plasmas using a plug-flow approximation, account for diffusion to surfaces, and incorporate changes in gas composition resulting from both heavy particle and electron impact processes. A detailed description of *GlobalKin* can be found in Lietz *et al* [11].

In summary, *GlobalKin* predicts species densities by integrating continuity equations that account for chemical reactions involving heavy particles and electron impact processes, diffusion to surfaces and surface chemistry, and gas flow. The gas temperature is computed using an energy conservation equation, which factors in Joule heating by the plasma, reaction enthalpies (both exothermic and endothermic), Franck–Condon heating, and heat transfer to the reactor walls through thermal conduction. The electron energy equation is solved separately to obtain the mean electron energy (or electron temperature).

Electron impact rate coefficients and transport coefficients are derived from solutions to Boltzmann's equation for the electron energy distribution across a range of reduced electric field values (E/N, electric field/gas density). These solutions generate a lookup table of transport and reaction rate coefficients as a function of the average electron energy. This table is then interpolated based on the current electron temperature and periodically updated during the simulation to reflect changes in gas composition.

The model uses a plug-flow approximation to address gas flow, which applies for subsonic, constant-pressure conditions where diffusion along the flow direction is negligible. The gas is tracked as it moves through the reactor as a fluid plug with a cross-sectional area equal to that of the reactor. The velocity of this gas plug is dictated by the initial flow rate, the gas density, and the reactor's cross-sectional area. Since reactions, gas inflow, and temperature variations affect the gas density, the plug speed is adjusted dynamically to maintain a stable pressure.

Power deposition by the plasma (W cm^{-3}) is defined as a function of position along the reactor length when using the plug-flow approximation. The power density profile is normalized such that its integral across the entire reactor matches the total specified power input. Along the reactor axis, power is evenly distributed except for the first and last millimeter of the reactor, where a ramp-up and ramp-down occur, respectively. No power dissipation occurs beyond the electrode boundaries.

The reaction mechanism used here consists of 101 gas-phase species and 2183 chemical reactions. The species included in the gas-phase mechanism are He, O_2, N_2, and H_2O, along with their associated ions, electronically excited states, and vibrationally excited species. More details regarding the gas-phase reaction mechanisms can be found in Lietz and Kushner [11] and Kruszelnicki *et al* [8]. Any deviations in reaction rate coefficients from these models are presented in the supplementary information table of Quesada *et al* [19].

The system parameters used in the model were chosen to represent the COST-Jet experimental conditions, including gas composition, flow rate and reactor dimensions. The gas plug was tracked as it traveled through the 30 mm length of the reactor, where its temperature increased by approximately 50 K while moving through the plasma before leaving the powered region. Upon exiting, the plasma effluent encountered ambient humid air or a nitrogen atmosphere, with ambient gases introduced into the plug flow to approximate interdiffusion between helium and the surrounding environment. At this stage, the gas temperature in the plasma plume rapidly dropped due to both thermal conduction and the entrainment of cooler ambient gas.

GlobalKin was used to investigate the effluent, region past the electrode/nozzle boundary, for the He/H_2O gas admixture as it flowed into air and nitrogen environments. The air and nitrogen atmospheres were simulated with initial molar compositions of $N_2/O_2/H_2O = 0.78/0.20/0.02$ and $N_2/H_2O = 0.98/0.02$, respectively [30].

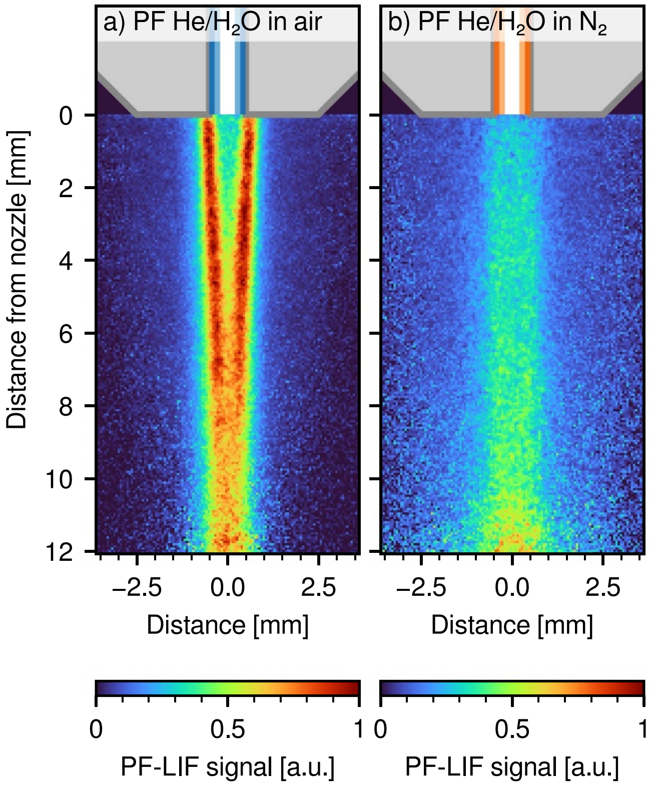

Figure 2. 2D PF-LIF signal distribution in an (a) air atmosphere and (b) N_2 atmosphere for the COST-Jet effluent with a He/H_2O admixture.

3. Mapping of H_2O_2 and HO_2 in the plasma effluent

3.1. Interpretation of the PF-LIF signal

The PF-LIF images of the COST-Jet effluent with a He/H_2O gas admixture recorded in air and N_2 environments are shown in figure 2. Each PF-LIF image is the difference between the OH-LIF signals with and without the pump laser. The PF-LIF signal is approximately 3% of the LIF signal from native OH in the effluent. Interpretation of PF-LIF signals from H_2O_2 and HO_2 is complicated by the fact that both molecules produce OH photofragments upon dissociation. For reactive flows that contain spatially overlapping mixtures of H_2O_2 and HO_2, the selective detection of each species using the PF-LIF technique is challenging. The signals from these species are separated by performing measurements in environments with and without oxygen exploiting the preferential formation of HO_2 in the presence of oxygen. The spatial distribution of the PF-LIF signal differs significantly depending on whether the effluent enters ambient air or nitrogen atmospheres, likely reflecting differences in contributions from these precursor molecules. Hydrogen peroxide and the hydroperoxyl radical are the primary precursor molecules produced by the plasma that photodissociate to produce ground-state OH radicals. The photoabsorption cross-sections for H_2O_2 and HO_2 at 213–216 nm are approximately 3.4×10^{-19} cm^2 and 3.5×10^{-18} cm^2, respectively, as shown in figure 3 [26, 27]. Contributions to

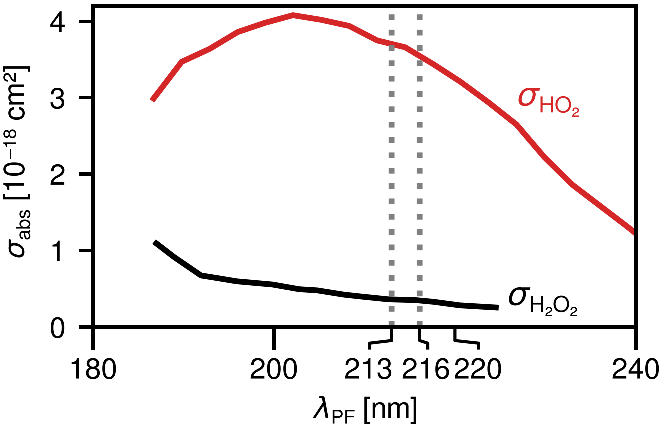

Figure 3. Absorption cross-section of H_2O_2 and HO_2 plotted as a function of laser wavelength from [26, 27].

the PF-LIF signal from water vapor are negligible, since the photoabsorption cross-sections for H_2O are on the order of 10^{-24} cm^2 or less in this spectral region at 292 K [31]. The absence of detectable PF-LIF signal from the 2500 ppm of water vapor in the jet when the plasma was turned off confirmed that contributions from water vapor were negligible.

The ratio of PF-LIF signals from H_2O_2 and HO_2 is given by:

$$\frac{S(H_2O_2)}{S(HO_2)} = \frac{n_{H_2O_2}}{n_{HO_2}} \cdot \left(\frac{\sigma_{H_2O_2} \cdot \phi_{H_2O_2}}{\sigma_{HO_2} \cdot \phi_{HO_2}}\right) \tag{1}$$

where n is number density, σ is absorption cross-section, and ϕ is the quantum yield of OH photofragments. The second ratio on the right-hand side of equation (1) is the relative detection efficiency of the PF-LIF signal for these two molecules:

$$\gamma = \frac{\sigma_{H_2O_2} \cdot \phi_{H_2O_2}}{\sigma_{HO_2} \cdot \phi_{HO_2}}. \tag{2}$$

The absorption cross-section of H_2O_2 is an order of magnitude smaller than that of HO_2. However, the quantum yield for OH production of H_2O_2 is twice that of HO_2 ($\phi_{H_2O_2} = 2$ and $\phi_{HO_2} = 1$ based on [32]). As a result, the relative detection sensitivity, γ, is approximately 0.2, indicating that the PF-LIF signal is about five times more sensitive to HO_2 than it is to H_2O_2. To determine when the PF-LIF signals in the COST-jet could contain significant contributions from both precursor molecules, the signal ratio in equation (1) was evaluated using the modeling results. The modeling results inform the analysis of the measured PF-LIF signals by providing an estimate of the number density ratio, $n_{H_2O_2}/n_{HO_2}$. The measurements are otherwise independent of the modeling results.

The modeling provides predictions of the H_2O_2 and HO_2 densities as a function of distance from the COST-jet nozzle exit for the nitrogen and air atmospheres, as shown in figure 4. In the N_2 atmosphere, the predicted H_2O_2 densities are consistently two orders of magnitude higher than those of HO_2. In this case, equation (1) yields a PF-LIF signal ratio of $S(H_2O_2)/S(HO_2) \sim 20$. That is, the PF-LIF signal from H_2O_2 is expected to be about 20 times larger than that of HO_2.

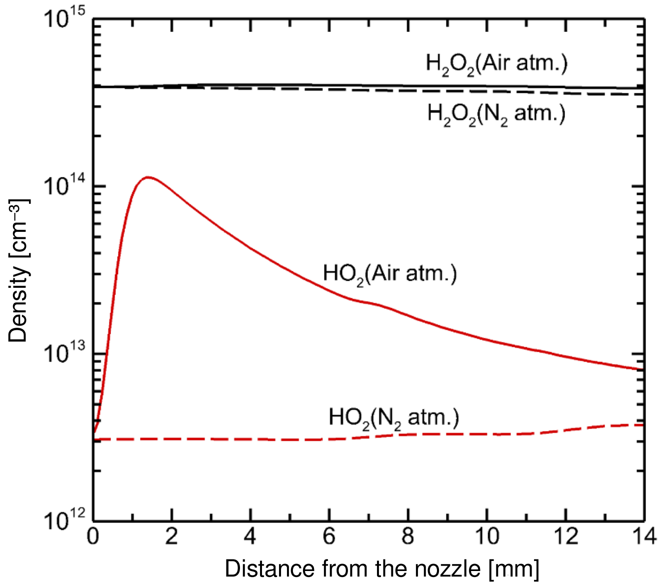

Figure 4. Model-predicted volume-averaged number densities of H_2O_2 and HO_2 as a function of distance from the COST-Jet nozzle for a He/H_2O admixture (1 slm, He/H_2O = 99.75/0.25) in both N_2 and air atmospheres.

In the air atmosphere, however, the predicted HO_2 densities are significantly larger, while the H_2O_2 densities are similar to those of the nitrogen atmosphere. Enhanced HO_2 formation can occur near the effluent–air interface through the three-body reaction:

$$H + O_2 + He \rightarrow HO_2 + He \tag{3}$$

where the production rate of HO_2 is limited by the availability of O_2 [19]. The predicted HO_2 number densities vary with downstream distance as air is entrained into the jet effluent. At the location of peak HO_2 density, the ratio of H_2O_2 and HO_2 densities is approximately 4. The predictions for the air atmosphere thus indicate that the PF-LIF signal ratio $S(H_2O_2)/S(HO_2)$ is expected to be of order unity, and therefore contributions from both molecules must be considered.

Based on the computational results, it is hypothesized that the PF-LIF signal from the COST-Jet effluent flowing into air contains contributions from both species and accordingly is referred to as $S(H_2O_2 + HO_2)_{air}$. In contrast, the suppression of HO_2 formation when flowing into the N_2 atmosphere results in a PF-LIF signal that is generated predominantly by H_2O_2 dissociation and is referred to as $S(H_2O_2)_{N_2}$. The H_2O_2 number density in the jet can be determined from measurements in the nitrogen atmosphere by

$$n_{H_2O_2,jet} = \frac{S(H_2O_2)_{N_2} \cdot Q_{N_2}}{S(H_2O_2)_{cal} \cdot Q_{cal}} \cdot n_{H_2O_2,cal} \tag{4}$$

where Q is the OH-LIF collisional quenching rate, and subscripts N_2 and cal refer respectively to the COST-jet with the N_2 atmosphere and the calibration measurements in which the six-way cross was filled with a uniform distribution of

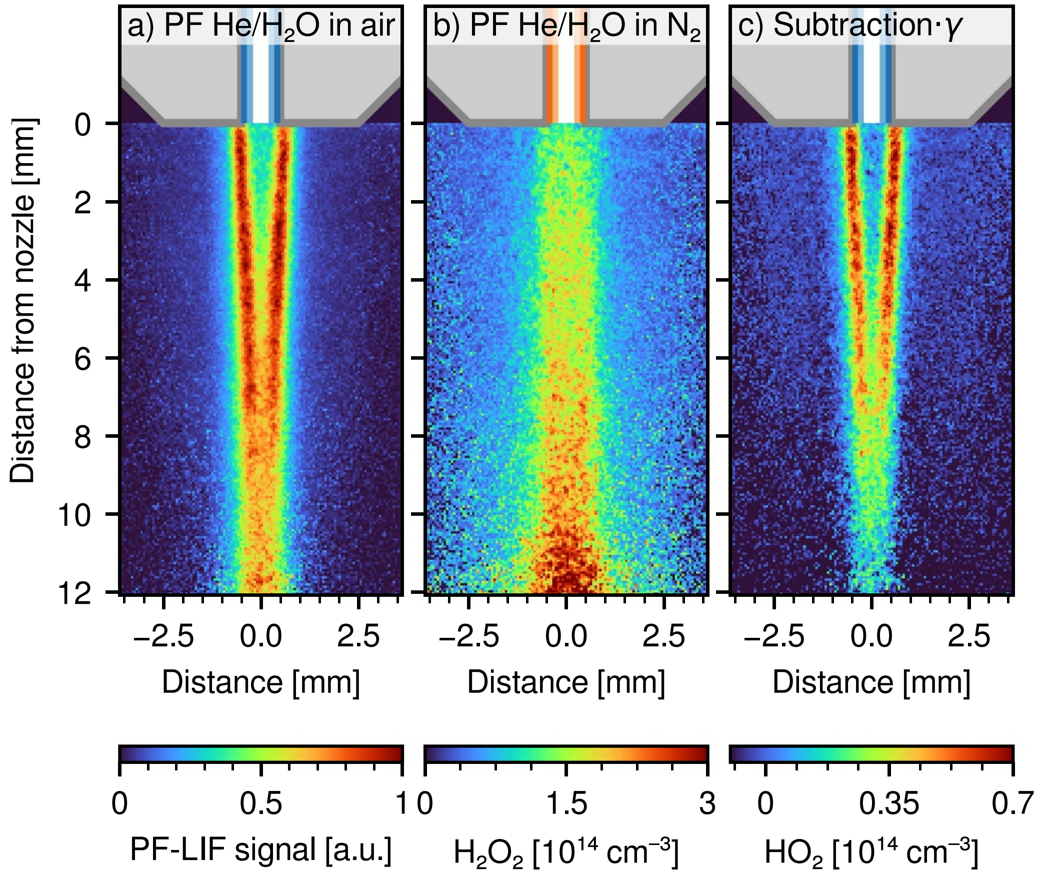

Figure 5. 2D PF-LIF measurements for the COST-Jet effluent with He/H_2O: (a) PF-LIF signal in air with contributions from both H_2O_2 and HO_2, (b) H_2O_2 density from PF-LIF signal in N_2, and (c) approximation of the HO_2 density in air determined from equation (5).

H_2O_2 vapor at a density of $n_{H_2O_2,\mathrm{cal}}$. In equation (4), factors that affect the OH-LIF signals such as the spectral overlap integral, optical collection efficiency, and detector sensitivity cancel out when calculating the ratio $S(H_2O_2)_{N_2}/S(H_2O_2)_{\mathrm{cal}}$ because the values of these factors are identical in the plasma and calibration measurements. The modeling results indicate that the expected H_2O_2 densities are nearly identical in the air and N_2 environments. As a result, the PF-LIF signal from HO_2 in the air atmosphere can be isolated by subtracting the signal in the nitrogen atmosphere to obtain the HO_2 number density:

$$n_{HO_2,\mathrm{jet}} = \frac{\left[S(H_2O_2+HO_2)_{\mathrm{air}}\cdot Q_{\mathrm{air}} - S(H_2O_2)_{N_2}\cdot Q_{N_2}\right]}{S(H_2O_2)_{\mathrm{cal}}\cdot Q_{\mathrm{cal}}}\cdot\gamma\cdot n_{H_2O_2,\mathrm{cal}} \tag{5}$$

where subscripts air and N_2 refer to data from the jet in the corresponding atmospheres, and the detection efficiency factor, γ, accounts for the differences in the absorption cross-sections and quantum yields of HO_2 and H_2O_2.

The OH-LIF collisional quenching rates, Q_{air} and Q_{N_2}, in equations (4) and (5) were measured on a pixel-by-pixel basis, as described in section 2.2. For each atmosphere and geometry, the corresponding quenching data were applied to correct the OH-LIF signal for both collisional quenching and associated VET/RET processes. Detection sensitivity depends strongly on the local quenching environment: in He-rich, low-quenching conditions relevant to this study, detection limits are estimated to be $10^{13}\,\mathrm{cm}^{-3}$ for H_2O_2 and $0.2\times10^{12}\,\mathrm{cm}^{-3}$ for HO_2, whereas in faster-quenching environments such as air or at high humidity, the limits increase by one to two orders of magnitude.

Using the relationships in equations (4) and (5), the contributions of HO_2 and H_2O_2 to the PF-LIF measurements can be separated. Spatial distributions are shown in figure 5 of (a) the PF-LIF signal in air, (b) the H_2O_2 density determined from the PF-LIF signal in N_2, and (c) the HO_2 density distribution in the air environment computed from equation (5). The H_2O_2 density (figure 5(b)) forms a stable column over most of the imaged region, consistent with model predictions of uniform H_2O_2 densities. In contrast, the V-shaped regions of large PF-LIF signal intensity in figure 5(a) are reflected in the HO_2 density map in figure 5(c). These regions at the periphery of the plasma effluent are interpreted as ‘reaction fronts’ where HO_2 forms as the plasma effluent containing H atoms interacts with ambient air containing O_2. The reaction fronts merge at approximately 8 mm downstream of the nozzle, and the HO_2 density gradually decreases with increasing distance from the nozzle.

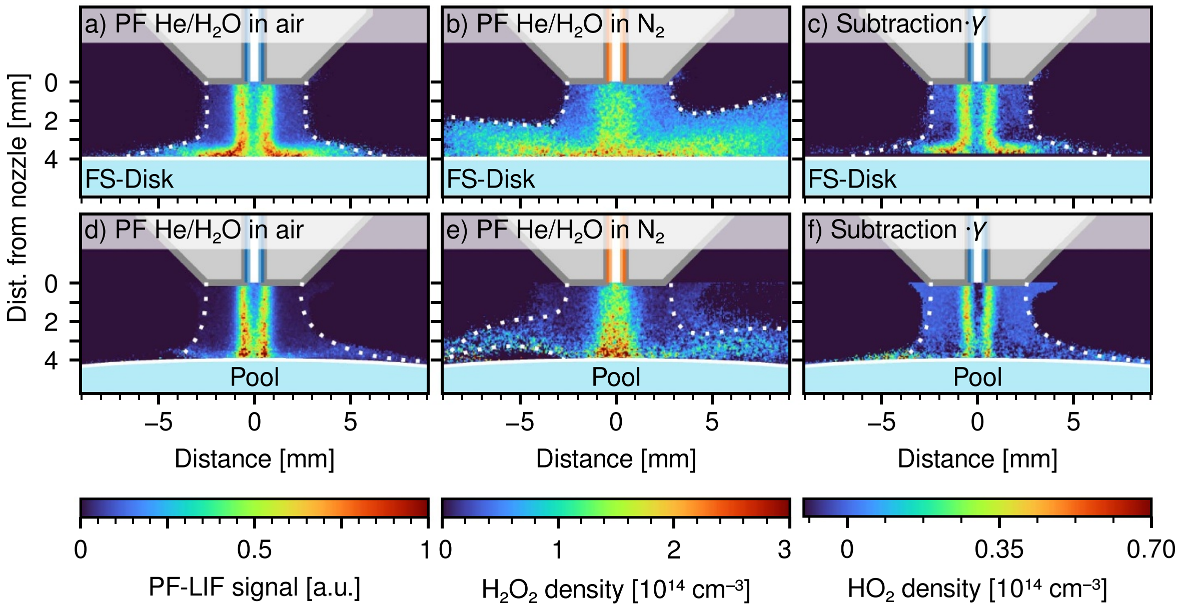

Figure 6. 2D PF-LIF measurements for the He/H_2O COST-Jet effluent interacting with solid and liquid targets. (a)–(c) Plasma effluent interacting with a FS disk: (a) PF-LIF signal in air (H_2O_2 + HO_2 contributions), (b) H_2O_2 density in N_2, and (c) approximation of HO_2 density in air atmosphere. (d)–(f) Plasma effluent interacting with a water pool: (d) PF-LIF signal in air, (e) H_2O_2 density in N_2 atmosphere, and (f) approximation of HO_2 density in air. The dotted white lines indicate the boundaries of the regions within which collisional quenching data of excited-state OH are available, which is required for calibrated PF-LIF measurements.

Our previous study of OH densities in the COST-jet reported similar, though less pronounced features and revealed significant differences in OH densities in the COST-jet effluent when flowing into nitrogen and air atmospheres [19]. The current results corroborate the previous study's hypothesis that the formation of 'reaction fronts' in air is primarily attributed to reactions involving HO_2, generated when effluent species, dominantly H atoms, interact with O_2 in the surrounding air. Several OH-related production and consumption pathways analyzed in [19] also influence HO_2 formation.

When comparing the H_2O_2 and HO_2 measurements in figure 5 with the modeling results, the model predicts an H_2O_2 density of approximately 4×10^{14} cm^{-3} at the nozzle exit for both gas environments, while measurements in the N_2 atmosphere indicate a density of 1.6×10^{14} cm^{-3} at the nozzle, increasing to about 3×10^{14} cm^{-3} at 12 mm downstream. The measurements align well with measurements by Harris *et al* [17], who reported H_2O_2 densities of 1.4×10^{14} cm^{-3} at 3 mm from the nozzle using a similar He/H_2O admixture. Up to 20 mm from the nozzle, Harris *et al* [17] measured a nearly constant on-axis H_2O_2 density, with the density decreasing with further increase in distance from the nozzle. The present 2D imaging shows a slight increase of on-axis density up to 12 mm from the nozzle.

For HO_2, the model predicts a density of approximately 0.4–1×10^{14} cm^{-3} in air at 0.2–0.5 mm from the nozzle, compared to the measured value of 0.6×10^{14} cm^{-3} at the nozzle. Considering that the 0D model provides volume-averaged densities and the measurements involve approximations, the agreement is satisfactory. This consistency supports the approach of subtracting the PF-LIF signal measured in N_2 from the total PF-LIF signal measured in air to obtain a reliable approximation of the HO_2 density distribution.

The approximation, however, is not exact. This is evident from the small negative values observed in the HO_2 profiles, which are most likely attributable to native HO_2 present in the effluent even in the N_2 case, or to slight differences in the H_2O_2 distribution between the nitrogen and air conditions. The simulations in figure 4 were used to estimate the systematic error introduced by assuming negligible HO_2 contributions in the N_2 environment. These simulations indicate that native HO_2 in the N_2 effluent would generate a PF-LIF signal equivalent to an apparent H_2O_2 density of 1.5×10^{13} cm^{-3}. This contribution results in an overestimation of the H_2O_2 density by approximately 10%, with a correspondingly similar underestimation of the HO_2 density. Given the absence of established methods for directly measuring HO_2 in the effluent of plasma jets, this level of systematic uncertainty represents a reasonable error regime.

3.2. Measured gas densities of H_2O_2 and HO_2 when encountering a solid or liquid interface

Two-dimensional (2D) PF-LIF measurements of the COST-Jet effluent interaction with a FS disk (a)–(c) and a liquid water pool (d)–(f) are shown in figure 6. As these images span a wide lateral area, they include regions where OH collisional quenching rates could not be measured due to the lack of natively produced OH in those locations. The dotted white lines in figure 6 indicate the boundaries of the regions for which the native OH-LIF signal was sufficiently strong to reliably measure the LIF collisional quenching rates. The row of pixels

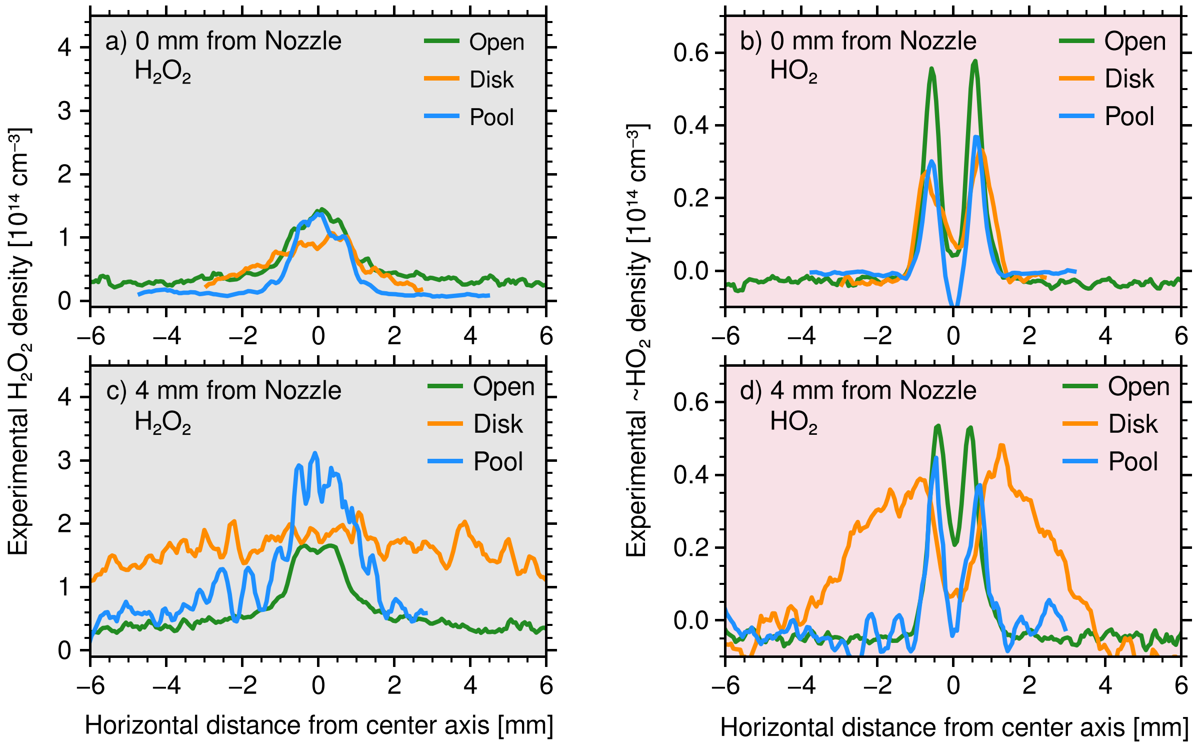

Figure 7. Horizontal profiles of measured H_2O_2 (a), (c) and HO_2 (b), (d) densities, derived from the 2D density maps in figures 5 and 6. The plasma effluent was examined under three conditions: no target (open), a solid target (FS disk), and a liquid target (water pool). Panels (a) and (b) depict data collected at the nozzle exit (0 mm), while (c) and (d) are 4 mm from the jet nozzle.

closest to the pool surface for which reliable data are available is 150 μm from the surface, which is indicated by the pool overlay in the images.

The measurements indicate that while the overall densities of estimated H_2O_2 and HO_2 remain comparable across the open effluent (figure 5), solid, and liquid target cases, the spatial distribution of these species is notably affected. The radial deflection of the stagnation flow produced by the jet impinging on a surface is pronounced for the FS disk. The reaction fronts in the PF-LIF signal in air (figure 6(a)) deflect outward upon contact with the solid surface, resulting in lateral redistribution of reactive species. This deflection pattern is evident in both the H_2O_2 (figure 6(b)) and the HO_2 (figure 6(c)) distributions. The HO_2 and H_2O_2 follow the same redirected transport pathway when approaching a solid surface, consistent with previously reported OH distribution patterns that followed the helium carrier gas flow [19]. The persistence of the densities of HO_2 and H_2O_2 in the deflected plumes suggests that neither species is significantly consumed at the solid surface.

In contrast, when the plasma effluent interacts with a liquid water pool (figures 6(d)–(f)), the reaction fronts appear to converge more rapidly toward the central axis as they approach the liquid surface. This effect is evident in the combined PF-LIF signals in air (figure 6(d)) and therefore the HO_2 distribution (figure 6(f)). The absence of lateral deflection of the reaction fronts suggests that the high-humidity boundary layer or liquid interface significantly absorbs or reacts with HO_2, effectively removing it from the gas phase. HO_2 does not rapidly react with H_2O vapor at ambient temperatures (6.04×10^{-35} cm^3/molecule·s [33]) but does have a large Henry's law coefficient ($H_s^{cc} = 1.69 \times 10^4$ [34]) for solvation into water. For H_2O_2, solvation into the liquid could play a larger role as its Henry's law coefficient ($H_s^{cc} = 2.13 \times 10^7$ [34]) is 100–1000 times larger than that for HO_2.

To facilitate quantitative comparisons between the solid-target, liquid-target, and no-target conditions, horizontal profiles of H_2O_2 (a), (c) and HO_2 (b), (d) densities are presented in figure 7. These profiles are extracted from the 2D density maps in figures 5 and 6 at two axial positions: 0 mm (the jet nozzle exit) and 4 mm (distance of the disk or pool from the jet nozzle).

The horizontal distributions of H_2O_2 densities at 0 mm from the nozzle (figure 7(a)) are similar when flowing into the open ambient and when the effluent impinges on solid and liquid targets. A similar trend is observed for HO_2 (figure 7(b)) although the open effluent case has a larger peak HO_2 density than the cases with targets. These similarities suggest that, within the limits of experimental uncertainty, the presence of a surface does not significantly alter the species densities at the nozzle exit.

Significant differences in densities occur at the 4 mm distance. In both the H_2O_2 and HO_2 profiles, the solid-disk scenario shows a broader lateral expansion, resulting in a more uniform distribution of these species, especially for H_2O_2. In contrast, the liquid pool gives rise to higher center-line H_2O_2 densities and a narrower horizontal distribution. Gaseous OH produced by interactions of RONS with water vapor, whose density increases towards the surface, could further drive OH–OH recombination into H_2O_2, a process that occurs with a high rate coefficient of 1.7×10^{-17} m^3 s^{-1} [35]. In the three-body mediated OH recombination reaction (OH + OH + M $\rightarrow$ H_2O_2 + M), the third-body efficiency of water is 5 to 6 times larger than that of N_2 and 12 times larger than that of He, which would further enhance H_2O_2 production near the liquid surface [36–38].

The high Henry's law coefficient for H_2O_2 ($H_s^{cc} = 2.13 \times 10^7$ [34]) suggests a significant portion of the H_2O_2 reaching the liquid surface solvates into the liquid. Assuming that the water is far from saturated with H_2O_2, so that all H_2O_2 at the water surface solvates, combining the average near-surface H_2O_2 density of 2×10^{14} cm^{-3}, at 4 mm from the nozzle, with the 1 slm jet flow rate, yields an H_2O_2 molecular throughput of 3.3×10^{15} molecules/s. This flux aligns well with the 240 μM H_2O_2 density observed at one minute of treatment in water samples treated 4 mm from the nozzle, corresponding to 2.42×10^{15} H_2O_2 molecules/s [39, 40] needed to impinge on the surface.

These observations suggest that introducing a solid versus a liquid target can dramatically alter the transport and fate of H_2O_2 in plasma effluents. One practical consequence is that in liquid treatments, such as when cells are in a Petri dish, the distance from the jet axis may influence exposure to plasma-generated species and therefore overall biological effects will vary, more than in analogous solid-surface treatments.

4. Conclusions

This study presents a method to map the spatial distribution of absolute H_2O_2 densities and to estimate HO_2 density distributions in the effluent of the COST atmospheric-pressure plasma jet operated with a He/H_2O admixture. Near the nozzle, densities of 1.6×10^{14} cm^{-3} for H_2O_2 and 0.6×10^{14} cm^{-3} for HO_2 resemble the 0D plasma chemistry model predictions. HO_2 is found mostly in 'reaction fronts' surrounding the effluent interacting with air.

Near-surface measurements reveal that while total species densities are comparable across all cases, their distribution is shaped by the target material. A solid surface results in lateral redistribution of species that is less pronounced than with a liquid interface, possibly due to the enhanced solvation or reaction with the liquid. H_2O_2 is particularly sensitive to these boundaries, forming a broad layer across solid surfaces while possibly solvating and accumulating in liquids. HO_2 shows smaller changes when targets are involved, potentially due to its lower solubility, shorter lifetime, and faster reaction kinetics.

These results highlight the critical role of boundary conditions in the transport of ROS and underscore the importance of carefully selecting and controlling target interfaces to tailor reactive species distributions for optimized performance in biological and chemical systems.

Data availability statement

All data that support the findings of this study are included within the article (and any supplementary files) and are available from the corresponding author upon reasonable request.

Supplementary Information available at https://doi.org/10.1088/1361-6463/ae1300/data1.

Acknowledgment

The work of M J Herrera Quesada and K Stapelmann was supported by the U.S. Department of Energy, Office of Science, Office of Fusion Energy Sciences Opportunities in Frontier Plasma Science program under Award Number DE-SC-0021329 and the U.S. National Science Foundation under Grant No. PHY-2308857.

The work of J Polito and M J Kushner was supported by the U.S. National Science Foundation (CBET-2032604), and the U.S. Department of Energy Office of Fusion Energy Sciences (DE-SC-0020232).

This research used resources of the Low Temperature Plasma Research Facility at Sandia National Laboratories, which is a collaborative research facility supported by the U.S. Department of Energy, Office of Science, Office of Fusion Energy Sciences.

Sandia National Laboratories is a multimission laboratory managed and operated by National Technology & Engineering Solutions of Sandia, LLC, a wholly owned subsidiary of Honeywell International Inc. for the U.S. Department of Energy's National Nuclear Security Administration under Contract DE-NA0003525. This paper describes objective technical results and analysis. Any subjective views or opinions that might be expressed in the paper do not necessarily represent the views of the DOE or the U.S. Government. The publisher acknowledges that the U.S. Government retains a non-exclusive, paid-up, irrevocable, world-wide license to publish or reproduce the published form of this written work or allow others to do so, for U.S. Government purposes. The DOE will provide public access to results of federally sponsored research in accordance with the DOE Public Access Plan.

ORCID iDs

María J Herrera Quesada 0000-0002-8623-550X
Sebastian Pfaff 0000-0002-8528-9362
Jordyn Polito 0000-0003-3409-6007
Mark J Kushner 0000-0001-7437-8573
Katharina Stapelmann 0000-0002-2116-2661

References

[1] Graves D B 2012 The emerging role of reactive oxygen and nitrogen species in redox biology and some implications for plasma applications to medicine and biology *J. Phys. D: Appl. Phys.* **45** 263001

[2] Privat-Maldonado A Schmidt A, Lin A, Weltmann K-D, Wende K, Bogaerts A and Bekeschus S 2019 ROS from physical plasmas: redox chemistry for biomedical therapy *Oxi. Med. Cell. Longevity.* **2019** 9062098

[3] Yayci A , Baraibar A G, Krewing M, Fueyo E F, Hollmann F, Alcalde M, Kourist R and Bandow J E 2020 Plasma-driven in situ production of hydrogen peroxide for biocatalysis *ChemSusChem* **13** 2072–9

[4] Kogelheide F , Voigt F, Hillebrand B, Moeller R, Fuchs F, Gibson A R, Awakowicz P, Stapelmann K and Fiebrandt M 2020 The role of humidity and UV-C emission in the inactivation of B. subtilis spores during atmospheric-pressure dielectric barrier discharge treatment *J. Phys. D: Appl. Phys.* **53** 295201

[5] Bogaerts A, Yusupov M, Razzokov J and Van der Paal J 2019 Plasma for cancer treatment: how can RONS penetrate through the cell membrane? Answers from computer modeling *Frontiers Chem. Sci. Eng.* **13** 253–63

[6] Wenske S, Lackmann J-W, Bekeschus S, Weltmann K-D, Von Woedtke T and Wende K 2020 Nonenzymatic post-translational modifications in peptides by cold plasma-derived reactive oxygen and nitrogen species *Biointerphases* **15** 061008

[7] Bekeschus S, von Woedtke T, Emmert S and Schmidt A 2021 Medical gas plasma-stimulated wound healing: evidence and mechanisms *Redox Biol.* **46** 102116

[8] Kruszelnicki J, Lietz A and Kushner M 2019 Atmospheric pressure plasma activation of water droplets *J. Phys. D: Appl. Phys.* **52** 355207

[9] Laroussi M *et al* 2021 Low-temperature plasma for biology, hygiene and medicine: perspective and roadmap *IEEE Trans. Radiat. Plasma Med. Sci.* **6** 127–57

[10] von Woedtke T, Emmert S, Metelmann H-R, Rupf S and Weltmann K-D 2020 Perspectives on cold atmospheric plasma (CAP) applications in medicine *Phys. Plasmas* **27** 070601

[11] Lietz A M and Kushner M J 2016 Air plasma treatment of liquid covered tissue: long timescale chemistry *J. Phys. D: Appl. Phys.* **49** 425204

[12] Verreycken T, Mensink R, Van Der Horst R, Sadeghi N and Bruggeman P J 2013 Absolute OH density measurements in the effluent of a cold atmospheric-pressure Ar–H_2O RF plasma jet in air *Plasma Sources Sci. Technol.* **22** 055014

[13] Lu X *et al* 2022 Grand challenges in low temperature plasmas *Front. Phys.* **10** 1040658

[14] Yang Q, Qiao J-J, Cheng H and Xiong Q 2023 Plasma-liquid interactions: an experiment and simulation study on plasma dynamic behaviors near the gas–liquid interfacial layer *Plasma Sources Sci. Technol.* **32** 095013

[15] Benedikt J Schröder D, Schneider S, Willems G, Pajdarová A, Vlček J and Schulz-von der Gathen V 2016 Absolute OH and O radical densities in effluent of a He/H_2O micro-scaled atmospheric pressure plasma jet *Plasma Sources Sci. Technol.* **25** 045013

[16] Schröter S *et al* 2018 Chemical kinetics in an atmospheric pressure helium plasma containing humidity *Phys. Chem. Chem. Phys.* **20** 24263–86

[17] Harris B, Krös L, Nave A, Wagenaars E and Van Helden J 2023 The spatial density distribution of H_2O_2 in the effluent of the COST-Jet and the kINPen-sci operated with a humidified helium feed gas *Plasma Sources Sci. Technol.* **32** 115010

[18] Belmonte T and Bruggeman P 2025 Optical diagnostics of discharges in and in contact with liquids *Plasma Process. Polym.* **22** 2400213

[19] Quesada M J H Pfaff S, Polito J, Gall G, Kushner M J, Frank J H and Stapelmann K 2025 Two-dimensional mapping of absolute OH densities in an atmospheric pressure plasma effluent via planar laser-induced fluorescence: effects of He/H_2O and He/O_2 mixtures in N_2 and air, with and without solid targets *J. Phys. D: Appl. Phys.* **58** 175205

[20] Li B , Jonsson M, Algotsson M, Bood J, Li Z S, Johansson O, Aldén M, Tunér M and Johansson B 2013 Quantitative detection of hydrogen peroxide in an HCCI engine using photofragmentation laser-induced fluorescence *Proc. Combust. Inst.* **34** 3573–81

[21] Larsson K, Johansson O, Aldén M and Bood J 2014 Simultaneous visualization of water and hydrogen peroxide vapor using two-photon laser-induced fluorescence and photofragmentation laser-induced fluorescence *Appl. Spectrosc.* **68** 1333–41

[22] Johansson O, Bood J, Aldén M and Lindblad U 2008 Detection of hydrogen peroxide using photofragmentation laser-induced fluorescence *Appl. Spectrosc.* **62** 66–72

[23] van den Bekerom D, Tahiyat M M, Huang E, Frank J H and Farouk T I 2023 2D-imaging of absolute OH and H_2O_2 profiles in a He–H_2O nanosecond pulsed dielectric barrier discharge by photo-fragmentation laser-induced fluorescence *Plasma Sources Sci. Technol.* **32** 015006

[24] Golda J *et al* 2016 Concepts and characteristics of the 'COST reference microplasma jet *J. Phys. D: Appl. Phys.* **49** 084003

[25] van den Bekerom D, Tahiyat M M, Huang E, Frank J H and Farouk T I 2023 2D-imaging of absolute OH and H_2O_2 profiles in a He–H_2O nanosecond pulsed dielectric barrier discharge by photo-fragmentation laser-induced fluorescence *Plasma Sources Sci. Technol.* **32** 015006

[26] Holt R, McLane C and Oldenberg O 1948 Erratum: ultraviolet absorption spectrum of hydrogen peroxide *J. Chem. Phys.* **16** 638–638

[27] Maricq M M and Szente J J 1994 A kinetic study of the reaction between ethylperoxy radicals and HO_2 *J. Phys. Chem.* **98** 2078–82

[28] Alkhalifa A M , Di Sabatino F, Steinmetz S A, Pfaff S, Huang E, Frank J H, Kliewer C J and Lacoste D A 2024 Quantifying the thermal effect and methyl radical production in nanosecond repetitively pulsed glow discharges applied to a methane-air flame *J. Phys. D: Appl. Phys.* **57** 385204

[29] Pfaff S, Huang E and Frank J H 2024 Imaging gas-phase methyl radicals over a Ag/SiO_2 catalyst during the partial oxidation of methanol *ACS Catalysis* **14** 15590–8

[30] Polito J and Kushner M J 2024 A hierarchal model for bacterial cell inactivation in solution by direct and indirect treatment using cold atmospheric plasmas *J. Phys. D: Appl. Phys.* **57** 405207

[31] Ranjan S , Schwieterman E W, Harman C, Fateev A, Sousa-Silva C, Seager S and Hu R 2020 Photochemistry of anoxic abiotic habitable planet atmospheres: impact of new H_2O cross sections *Astrophys. J.* **896** 148

[32] Vaghjiani G L and Ravishankara A R 1992 Photodissociation of hydrogen peroxide at 193 nm and 248 nm: quantum yields for OH and O(1D) products *J. Chem. Phys.* **97** 7031–43

[33] Lloyd A C 1974 Evaluated and estimated kinetic data for phase reactions of the hydroperoxyl radical *Int. J. Chem. Kinet.* **6** 169–228

[34] Sander R 2023 Compilation of Henry's law constants (version 5.0. 0) for water as solvent *Atmos. Chem. Phys.* **23** 10901–12440

[35] Poggemann H-F, Schüttler S, Schöne A L, Jeß E, Schücke L, Jacob T, Gibson A R, Golda J and Jung C 2025 Transportation behaviour of OH and H_2O_2 in plasma-treated water *J. Phys. D: Appl. Phys.* **58** 135208

[36] Zellner R, Ewig F, Paschke R and Wagner G 1988 Pressure and temperature dependence of the gas-phase recombination of hydroxyl radicals *J. Phys. Chem.* **92** 4184–90
[37] Sellevåg S R, Georgievskii Y and Miller J A 2009 Kinetics of the gas-phase recombination reaction of hydroxyl radicals to form hydrogen peroxide *J. Phys. Chem. A* **113** 4457–67
[38] Troe J 2011 The thermal dissociation/recombination reaction of hydrogen peroxide $H_2O_2(+M) \leftrightarrow 2OH(+M)$ III.: analysis and representation of the temperature and pressure dependence over wide ranges *Combust. Flame* **158** 594–601
[39] Stapelmann K, Myers B, Quesada M H, Lenker E and Ranieri P J 2021 Following O and OH in He/O_2 and He/H_2O gas mixtures—from the gas phase through the liquid phase to modifications on a biological sample *J. Phys. D: Appl. Phys.* **54** 434003
[40] Myers B, Barnat E and Stapelmann K 2021 Atomic oxygen density determination in the effluent of the COST reference source using in situ effective lifetime measurements in the presence of a liquid interface *J. Phys. D: Appl. Phys.* **54** 455202